Communication

Experimental Investigation of Meter-Level Resolution Radar Measurement at Ka Band in Yellow Sea

Xiaoxiao Zhang [1,*], **Xiang Su** [2], **Lixia Liu** [2] **and Zhensen Wu** [3]

1   School of Electronic Engineering, Xi'an University of Posts & Telecommunications, Xi'an 710121, China
2   China Academy of Space Technology, Xi'an 710100, China; xiang_su@stu.xidian.edu.cn (X.S.);
    liulx@cast504.com (L.L.)
3   School of Physics, Xidian University, Xi'an 710071, China; wuzhs@mail.xidian.edu.cn
*   Correspondence: zhangxiaoxiao@xupt.edu.cn

Abstract: The backscatter characteristics of ocean surfaces are of great importance in active marine remote-sensing fields. This paper presents the high spatial and temporal resolution dual co-polarized (VV and HH) and cross-polarized (HV) Ka-band sea-surface backscattering measurements taken from the Yellow Sea research platform at incidence angles ranging from 30° to 50° and in the wind speed range from 5.8 to 8.6 m/s. The experimental results show that the backscattering coefficient in HH polarization is close to (or even surpassing) that in VV polarization within a wind speed range of 7.1 to 8.6 m/s for Ka band under high resolution at medium incidence angles (30°–50°). Further analysis of the 10-ms short-time observation samples found that the sea surface echoes in VV polarization are more sensitive to wave motions, exhibiting more complex scattering characteristics such as multi-peaks and reducing scattering energy, especially at high wind speeds and large incident angles. The Doppler velocity analysis also confirms that rapid ocean wave changes can be detected within a short observation period, especially in VV polarization. The research in this article not only demonstrates the high spatial and temporal resolution capabilities of Ka-band radar for ocean surface observation but also reveals its great potential in interpreting and inversing rapidly evolving marine phenomena.

Keywords: high resolution; radar measurement; sea backscattering; doppler velocity

1. Introduction

Backscattering from the ocean's surface is critical in the application of active ocean remote-sensing, such as sea-state monitoring [1,2], surface current estimation [3], and target detection [4], to name a few. In the past few decades, exclusive research has been implemented both theoretically and experimentally in the L-, C-, X-, and Ku-band. However, the low spatial and temporal resolutions of the decimeter or centimeter radio bands' radar monitoring render it inadequate for detecting sub-mesoscale ocean phenomena. A demand for higher spatial resolution and the detection of ocean phenomena require the exploration of higher radar frequencies.

Benefiting from higher spatial resolution and a simpler system design, the Ka-band radar is attracting growing attention, such as radar altimeter for sea surface height (SSH) measurement and the estimation of snow cover thickness on sea ice, wind scatterometers, and Doppler scatterometry for simultaneous measurements of ocean-surface vector winds and currents. A Ku/Ka dual-band SAR altimeter airborne experiment was carried out over the South China Sea on 6 November 2021, demonstrating that the Ku/Ka precision ratio is possible to achieve 1.4 [5]. The surface water and ocean topography (SWOT) satellite, jointly developed by the National Aeronautics and Space Administration and the Centre National d'Études Spatiales (CNES), was successfully launched in December 2022. The Ka-band radar interferometer (KaRIn) carried by SWOT can provide 2-D sea surface height (SSH) data, enabling the acquisition of a high-precision and high-spatial-resolution

(2 cm@3 km × 3 km) ocean gravity field [6,7]. Coincident radar measurements at Ku- and Ka-bands onboard a Twin Otter aircraft with ultra-wideband measurement capabilities can yield cm-scale vertical resolution for altimetry [8]. An accurate wind retrieval method has been developed for SWOT KaRIn 2 by 2-km pixel data. The new wind retrievals are consistent with ASCAT ocean-wind scatterometer wind speeds (1.00 m/s standard deviation) with a small bias (−0.25 m/s) for globally distributed observations of small-scale ocean wind processes [9]. The DopplerScatt airborne Doppler Scatterometer funded by NASA provides scientifically important measurements of ocean currents and winds (400 m resolution) and their derivatives (1 km resolution) over a 25 km swath.

By increasing the frequency, new scientific opportunities appear directly linked to the exploitation of the electromagnetic properties of the interaction between radar wave and surface [10,11]. At the Ka-band, radar scattering is caused by small wind-driven capillary waves (centimeter-scale) that are modulated by longer surface waves, breaking waves, and the underlying surface current. The Ka-band Doppler Scatterometer has successfully demonstrated its ability to sense submesoscale ocean vector winds and currents that were previously impossible to sense, which is recognized as a promising new approach for obtaining joint measurements of winds and currents [12,13]. Ku-Ka band Interferometric SAR altimetry is considered to be the optimal choice for the next generation of altimeters, with a significantly improved temporal and spatial resolution up to days and kilometers [14–16], respectively.

For Ka-band measurements, wave motions that are sensitive to wave-wind, wave-current, and wave-bottom interactions can be well traced. The backscattering cross-section and Doppler shifts, compared to the coverage of the radar footprint from the Black Sea research platform, are presented through joint Ka-band dual co-polarized radar and video observations [17]. The sea surface backscatter properties are analyzed to assess the impact of sea spray on the Ka-band backscatter cross-section and its Doppler characteristics during a strong offshore wind event [18]. Additionally, the non-polarized features observed on the normalized radar cross-section, as well as Doppler velocities caused by large foaming and breaking waves resolved by the radar footprint, are examined [19–21]. Nevertheless, physical understanding and modeling of Ka-band ocean-surface backscatter are challenging for the investigation of future applications due to a lack of high-resolution measurements with ocean meteorological parameters. In this study, we present the first investigation of Ka-band high-resolution backscattering characteristics surveys over the Yellow Sea, close to Yantai coast, including two main interesting aspects associated with the presented measurement campaigns. The first one is the average scattering coefficient for long-duration observation associated with wind speed and direction. The second aspect is the rapid variations in sea surface echoes and Doppler velocities for short-duration observation.

This paper is organized as follows: the sea platform and the high-resolution radar measurement system, including the antenna components and transceiver timing sequence, are introduced in Section 2. Section 3 presents the analysis of the measurement data, including the temporal series of the scattering coefficient at the beam center and the average scattering coefficient over a duration of 20 s at different wind speeds, ranging from 5.8 to 8.6 m/s, in both co-polarization and cross-polarization. A detailed analysis and discussion of the rapid variations in sea surface echoes and Doppler velocities for short-duration observation samples of 10 ms at different incident angles and polarizations are presented in Section 4. The obtained results are summarized in Section 5.

2. Meter-Level Resolution Radar System

The measurement was carried out on the offshore platform that belongs to the National Satellite Ocean Application Center of China in July 2021. The platform is located about 50 nautical miles north of Yangma Island in the Yellow Sea and equipped with the capability for continuous 24-h monitoring of wind speed and direction. The antenna direction is oriented 100° clockwise from the north for observation of sea surface driven by the SE wind. The platform is far away from the mainland; therefore, the radar echo is less disturbed by land clutter. Additionally, during the measurement period, no ships passed by due to the

fishing moratorium, and all irrelevant electronic equipment on the platform was turned off in order to minimize the interference of electronic devices on the measurement. During the measurement, foam and wave breaking could be observed, as shown in Figure 1.
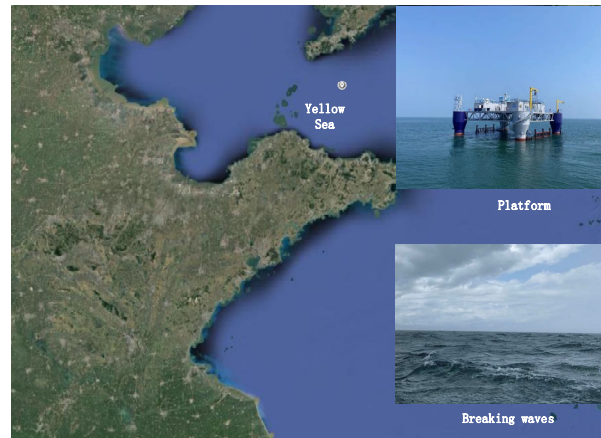

Figure 1. Offshore platform.

The measurement system, as depicted in Figure 2, comprises a control and acquisition unit, a transmitter and receiver unit, a microwave front-end, an antenna system, a servo system, and a power distribution unit. This system enables the configuration of pulse width, frequency, polarization, and timing sequences.
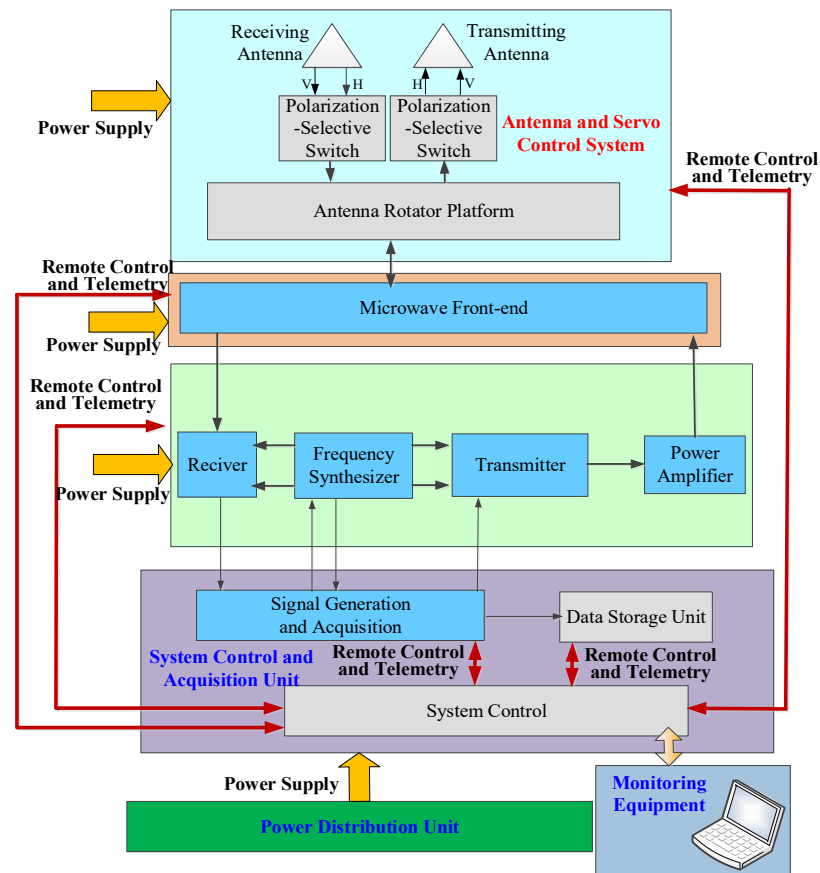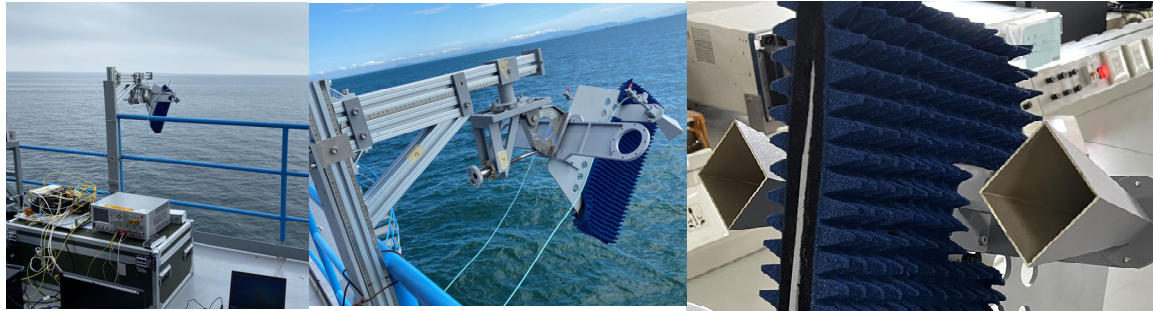

Figure 2. Measurement system.

2.1. Antenna Assemble

The antenna is mounted on a support structure, positioned at a height of 8.6 m above sea level. The antenna utilizes a horn transmitter to illuminate the ocean surface. We used electromagnetic absorbing foam in select locations to maximize the isolation between the radar antennas, and thereby reduce short-range leakage between the transmitter and receiver, as shown in Figure 3.
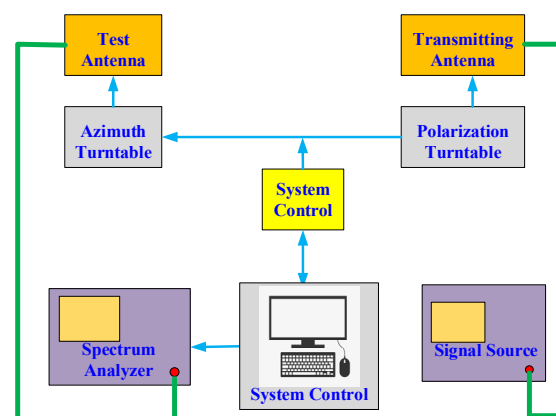

Figure 3. The radar system and antenna.

The measurement system undergoes parameter calibration, which includes antenna gain, 3 dB beamwidth, antenna receive-transmit (R/T) isolation, and polarization isolation. The antenna parameters are measured in a microwave anechoic chamber with the distance R between the transmitting and receiving antennas satisfying the far-field conditions. The equipment used for antenna parameter calibration is shown in Table 1.

Table 1. Equipment for testing antenna parameters.

Number	Equipment Name	Equipment Model	Serial Number
1	Vector Network Analyzer	Agilent 8722ET	US39175028
2	Spectrum Analyzer	MS2667C	6200071090
3	Signal Source	N5183A	MY50140986

The antenna pattern measurement system, as depicted in Figure 4, comprises the spectrum analyzer, signal source, turntable, test antenna and transmitting antenna. The signal generator is set to a single-frequency mode. A standard gain horn is used for transmission. We can obtain the antenna patterns as well as the antenna gain and 3 dB beamwidth for both the E-plane and the H-plane of the antennae from the spectrum analyzer. The antenna patterns of the Ka-band antenna in V-polarization and H-polarization are shown in Figure 5.

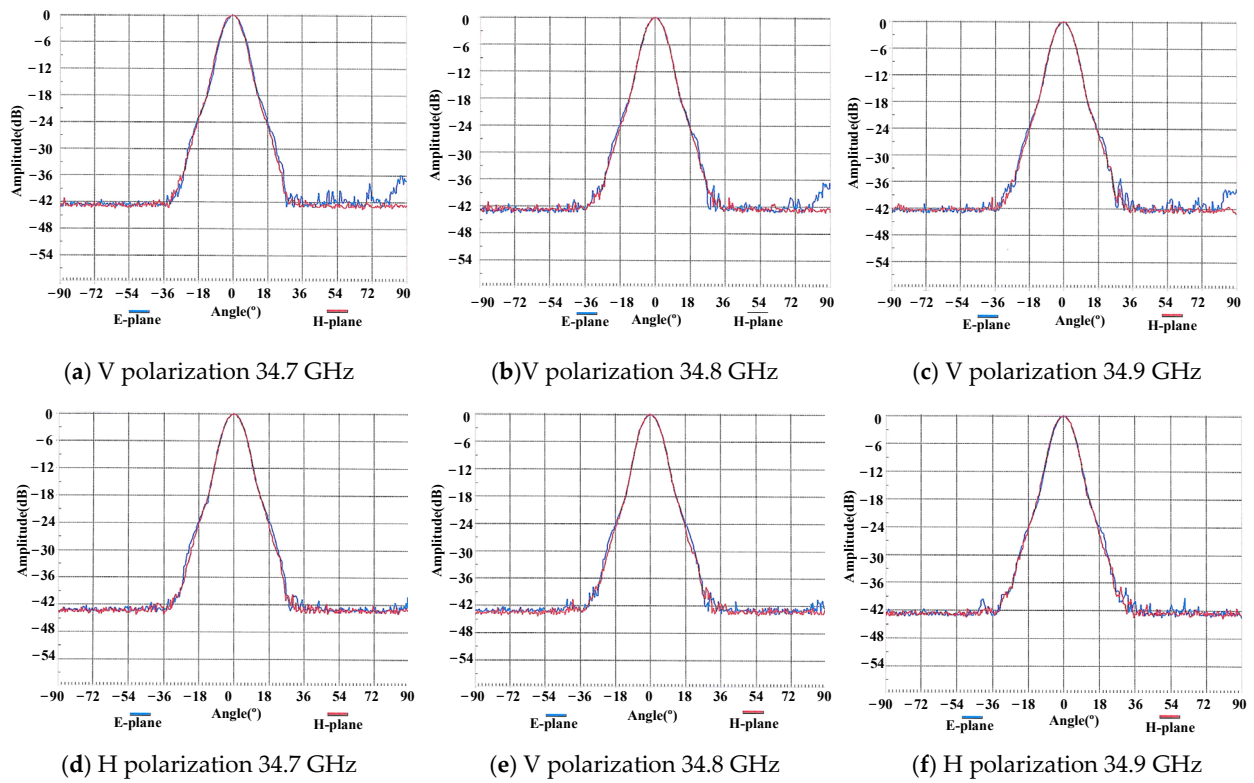**Figure 4.** The antenna pattern measurement system.

(**a**) V polarization 34.7 GHz   (**b**)V polarization 34.8 GHz   (**c**) V polarization 34.9 GHz

(**d**) H polarization 34.7 GHz   (**e**) V polarization 34.8 GHz   (**f**) H polarization 34.9 GHz

Figure 5. The antenna patterns of the Ka-band antenna.

Polarization isolation can be obtained by the following steps: Align the transmitting and receiving antennas to face each other. When the transmitting and receiving antennas are co-polarized, record the received signal level. Then, switch the transmitting antenna to cross-polarization and record the received signal level again. The difference between the two received signal levels is the polarization solation of the receiving antenna. The polarization isolation antenna patterns of the Ka-band antenna are shown in Figure 6.
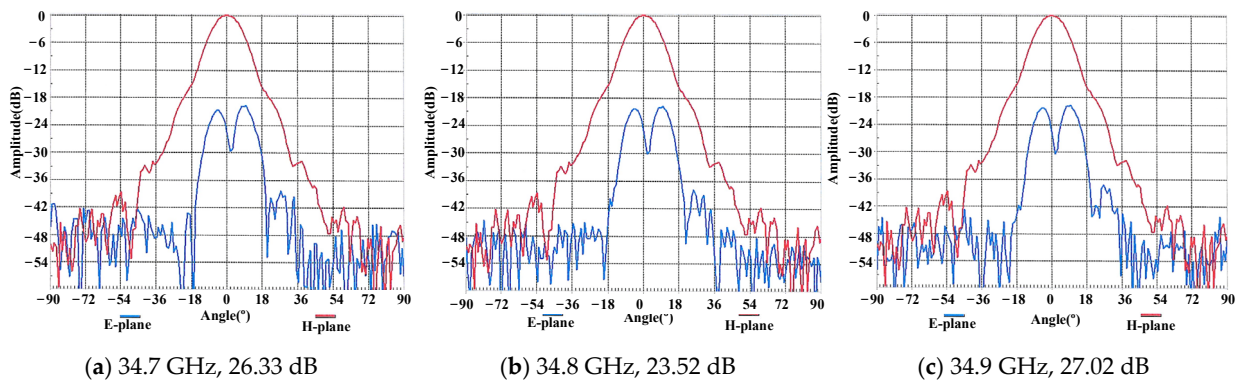

(**a**) 34.7 GHz, 26.33 dB   (**b**) 34.8 GHz, 23.52 dB   (**c**) 34.9 GHz, 27.02 dB

Figure 6. The antenna patterns for polarization isolation.

The antenna receive–transmit (R/T) isolation is obtained using the Vector Network Analyzer by measuring the S21 parameter of the antenna. The measured isolation of the transmission antenna is −109.26 dBm. The detailed antenna parameters are outlined in Table 2.

Table 2. Antenna parameters.

Frequency (GHz)	Polarization	Gain (dB)	3 dB Beamwidth in E Plane (°)	3 dB Beamwidth in H Plane (°)	Sidelobe in E Plane (dB)	Sidelobe in H Plane (dB)
34.7	V	24.61	9.96	9.64	−37.85	−36.09
34.8	V	24.84	10.03	9.99	−37.11	−37.16
34.9	V	25.09	9.40	9.80	−35.07	−35.48
34.7	H	24.55	10.12	9.88	−38.23	−39.56
34.8	H	24.78	9.91	9.95	−37.76	−36.83
34.9	H	24.98	9.51	9.91	−36.87	−36.74

2.2. Transmitting and Receiving Signals

The radar transmits a linear frequency modulated (LFM) signal, i.e.,

$$s(t) = rect(\frac{t}{T_p}) \exp(j2\pi f_c t) \exp(j\pi K t^2), \tag{1}$$

where t is the fast time, $f_c = 600$ MHz, and K is the chirp rate of the signal. The transmitted LFM signal boasts a bandwidth of 150 MHz and a time duration of 100 μs, achieving a resolution of 1 m level after pulse compression. The sampling rate of the data acquisition system is 480 MHz. Figure 7 illustrates the transmission and reception timing.
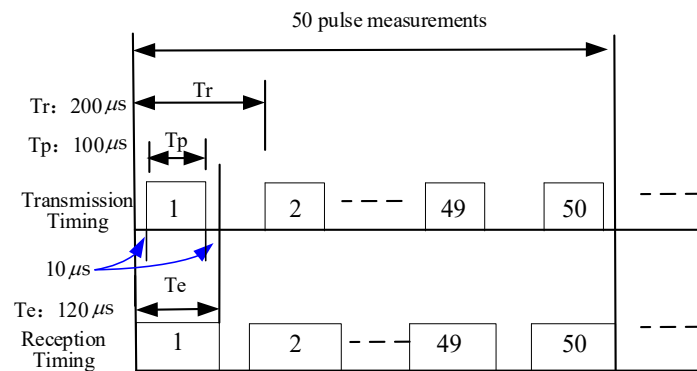
Figure 7. Transmission and reception timing.

- Transmission timing

The pulse duration is 100 μs, and the pulse repetition interval (PRI) is 200 μs.

- Reception timing

The receiver is powered on 10 μs prior to the transmitter and deactivated with a 10 μs delay to compensate for potential delays in the receiver link. Consequently, the receiver pulse duration is set at 120 μs, while the PRI remains at 200 μs.

3. Measurement Data

After preprocessing the acquired binary data, the raw signal is extracted. Subsequently, this raw data undergoes digital down-conversion, windowing, and pulse compression processing, resulting in a compressed signal with an enhanced signal-to-noise ratio (SNR). The SNR attains 60 dB after four accumulations in the range direction, as illustrated in Figure 8, enabling the effective extraction of sea-surface echo signals. We use the internal calibration method for the radar measurement. According to the internal calibration method and the radar equation, the backscattering coefficient of the sea surface can be calculated by the following formula:

$$\sigma = \frac{(4\pi)^3 R^4}{G^2 A \lambda^2} \frac{P_{\text{sea}}}{P_{\text{ref}} L_f}, \tag{2}$$

where R is the distance from the antenna to the center of the illuminated sea surface, and G is the antenna gain. A is the irradiation area of the sea surface, λ is the incident wavelength, and L_f is the load loss for internal calibration (L_f = 110 dB). P_{sea} is the echo power of the signal from sea surface, and P_{ref} is the reference echo power of the internal calibration signal.
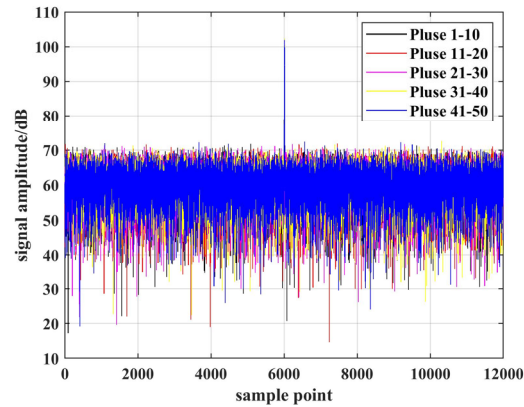
Figure 8. Compressed signal.

Figure 9 offers a snapshot of the backscattering coefficients of the sea surface illuminated by the beam center over a period of 20 s with a 30° incidence angle for HH and VV polarization. The bule line represents the instantaneous scattering coefficient, and the red line represents the average value over 20 s. We can observe that the backscatter coefficient for HH polarization is close to that for VV polarization. We also conducted measurements of the sea-surface backscatter coefficient in cross-polarization for 50.5° incidence, as shown in Figure 10. Specifically, at a fixed incident angle of 50.5°, under identical wind-speed conditions, the backscatter coefficient in HV polarization is approximately 20 dB lower than that in VV polarization. We provide a more exhaustive dataset for the average sea-surface backscattering coefficients with time intervals of 20 s and 200 s under various incident angles and polarization in Table 3. We found that the differences between the backscattering coefficients with time intervals of 20 s and 200 s are less than 2 dB, which can be negligible. Furthermore, the table includes the sea-surface wind speed and direction at 16 m above sea level during the measurement, which are essential for elucidating the intricate relationship between the scattering characteristics and oceanic conditions.

(**a**)   (**b**)
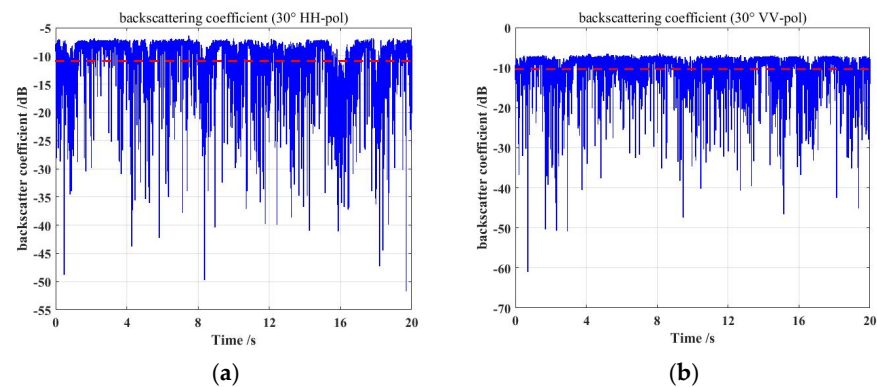
Figure 9. Backscatter coefficient of sea surface with 30° incidence: (**a**) 30° incidence, HH polarization and (**b**) 30° incidence, VV polarization.

It is known that for large-area statistical sea-surface observation, Bragg scattering from the sea surface dominates at medium incidence angles (30°–60°). Generally, the backscattering coefficient of the sea surface in VV polarization is greater than HH polarization under the same wind speed. As the wind speed increases, the sea surface becomes rougher, which enhances the interaction between radar waves and the sea surface, leading to an increase

in the backscatter coefficient. The backscatter coefficient in HH polarization surpasses that in VV polarization, which usually occurs at small grazing angles with high wind speed. However, during this measurement, an intriguing phenomenon emerged: at the medium incidence angle, the backscatter coefficient in HH polarization was close to (or even surpasses) by that in VV polarization within a wind speed range of 7.1 to 8.6 m/s. We compared the observational data with the slope-deterministic, facet-based two-scale model (SDFb-TSM), the modified SDFb-TSM with breaking waves and foam developed in our previous work [22,23], and published data [24], as shown in Figure 11a.
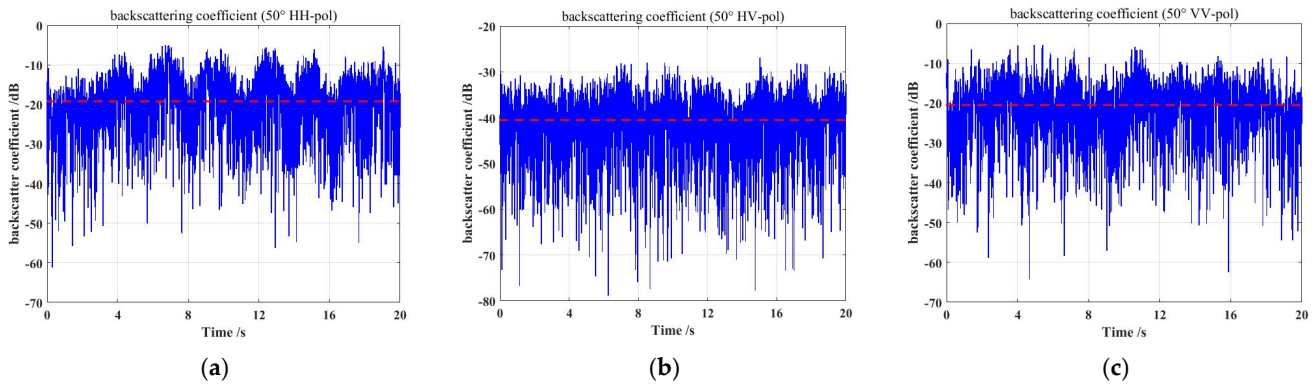

Figure 10. Backscatter coefficient of sea surface with 50.5° incidence: (**a**) HH polarization, (**b**) HV polarization, and (**c**) VV polarization.

Table 3. Measurement parameters and results.

| Incident Angle (degree)	Polari -Zation	Wind Speed (m/s)	Wind Direction (degree)	Backscatter Coefficient (dB) Time Interval 20 s	Backscatter Coefficient (dB) Time Interval 200 s	Bimodal Percentage
30	HH	8.6	147	−10.883	−10.006	5.38%
30	VV	8.1	143	−10.347	−9.495	7.6%
35	HH	7.5	149	−12.476	−13.978	7.18%
35	VV	8.3	147	−15.037	−14.146	9.04%
40	HH	7.2	145	−15.362	−17.942	8.75%
40	VV	7.9	146	−16.259	−16.231	9.16%
45	HH	7.4	144	−16.405	−18.335	8.96%
45	VV	7.1	147	−17.331	−17.383	10.3%
50.5	HH	7.7	145	−19.195	−19.941	/
50.5	HV	5.8	148	−40.560	−41.582	/
50.5	VV	5.9	146	−20.569	−20.440	/
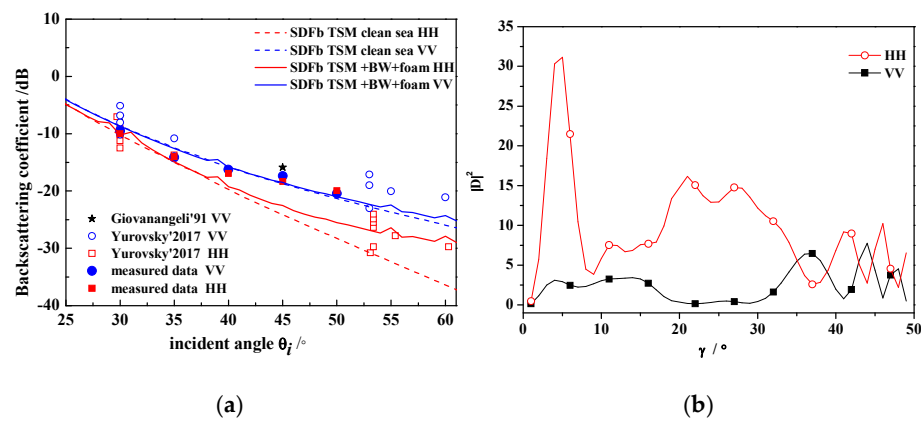
Figure 11. Measured backscattering coefficient and simulated result for sea and mesoscale wave. (**a**) Backscattering coefficient from sea surface; (**b**) $|D|^2$ versus grazing angle γ.

It can be observed that the VV polarization scattering is in good agreement with the experimental data. There is a significant difference between the scattering coefficient calculated using the SDFb-TSM model and the measurement results for HH polarization. By using the improved SDFb-TSM model while considering breaking waves, the scattering coefficient under HH polarization was enhanced as compared to that of the clean sea surface, but there was still a gap when compared to the measured data. Specifically, at a 45° and a 50° incidence angle, the measured scattering coefficient was 4 dB high and 5.5 dB higher, respectively, than the scattering model predicted. The polarization anomaly of sea surface scattering has been explained in many studies. These include the multipath effect of breaking waves and the surrounding sea surface [25], the damping effect at the Brewster angle for VV polarization [26], the volumetric scattering of foam [27], and the diffraction effects of wave crests [28]. In addition, high-resolution observations also contribute to this phenomenon. High temporal resolution observations enable us to capture the rapid variations of ocean motion on the sub-microsecond scale. High spatial resolution observations, on the other hand, allow us to detect sea waves on the meter scale. The scattering characteristics of such meter-scale waves are different from those obtained by averaging the entire sea surface for low-resolution observations. High-resolution observations of the sea surface are more capable of capturing local motion features, such as the rapid changes in the angle between the incident direction of the radar wave and the locally inclined surface. Therefore, the local incident angle may become larger or smaller than the global incident angle. A mesoscale breaking-wave model proposed by Churyumov and Kravtsov can explain this phenomenon [28]. The backscatter cross-section from a single breaking wave is determined by the diffraction coefficients $|D|^2$ of wave crest. We plotted the diffraction coefficients $|D|^2$ versus the grazing angle γ, as shown in Figure 11b. We can observe that, for the curved, wedge-like breaking waves at certain angles (especially at small grazing angles), the diffraction coefficients under HH polarization can be greater than those under VV polarization, with a maximum occurring at the Brewster angle. This results in the echo signal exhibiting double or even triple peaks, especially for high wind speed and large incident angles under VV polarization. Statistical analysis of the observation results reveals that, under similar wind speeds, the probability of a bimodal phenomenon is higher for VV polarization as compared to HH polarization, as shown in Table 3. The bimodal mode induces a weaker polarization ratio. We attribute this to the high spatio-temporal resolution observation, for which the radar captures more instantaneous variations of the tilted waves. For instance, tilt modulation accumulates the suppressive effect near the Brewster angle under VV polarization, while the single-peak mode under HH polarization remains relatively stable, with the scattering intensity approaching or even slightly exceeding that of VV polarization. Consequently, the polarization ratio in this observation is relatively weaker than in other studies. Instead of the long-term statistical behavior of large-area waves, we are more concerned with their instantaneous and local behaviors, which will be further analyzed in Discussion section below.

4. Discussion

In this section, we analyzed the short-duration observation (10 ms) for the sea-surface scattering characteristics. As shown in Figure 12, for a 35° incidence angle with HH polarization and a sea-surface wind speed of 7.5 m/s, the sea surface echo exhibits a stable single-peak signal throughout the short-term observation, indicating slow ocean wave changes. In contrast, with VV polarization and a higher sea-surface wind speed of 8.3 m/s, the wave motion on the sea surface changes more dramatically. Especially for pulses 41–50, sea waves may break, resulting in a double-peak in the sea surface echo, with the peak corresponding to a range offset from the radar beam center. The amplitude of the sea surface echo decreases significantly, with the maximum value dropping by approximately 15 dB.
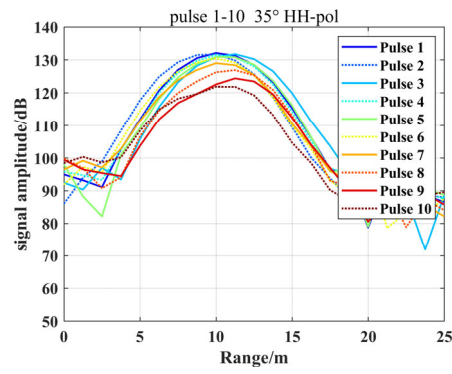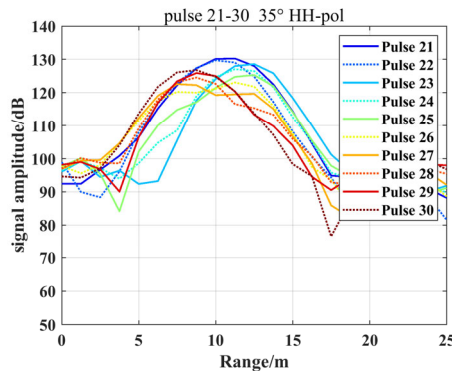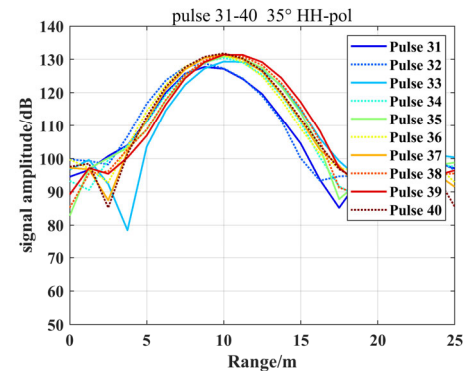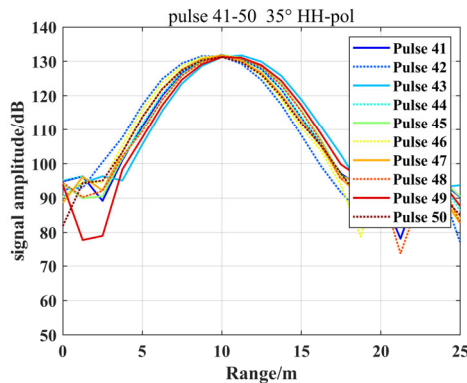
(**a**) pulse 1–10, HH polarization
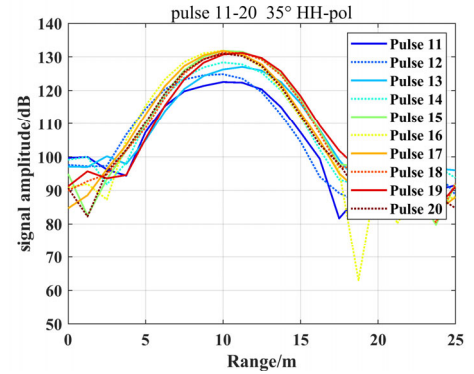
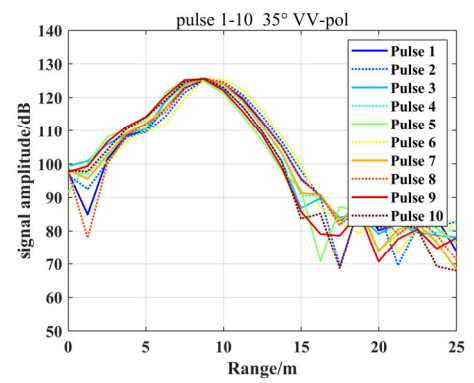(**b**) pulse 11–20, HH polarization

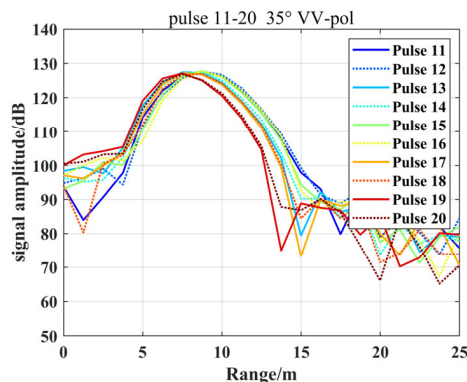(**c**) pulse 21–30, HH polarization
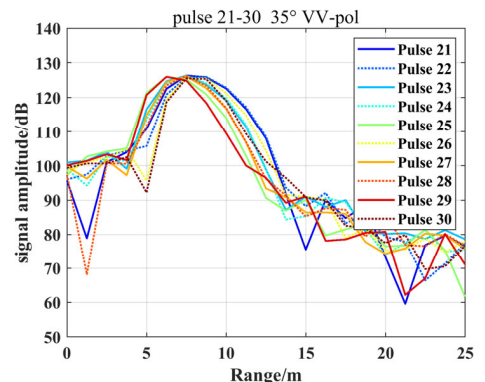
(**d**) pulse 31–40, HH polarization

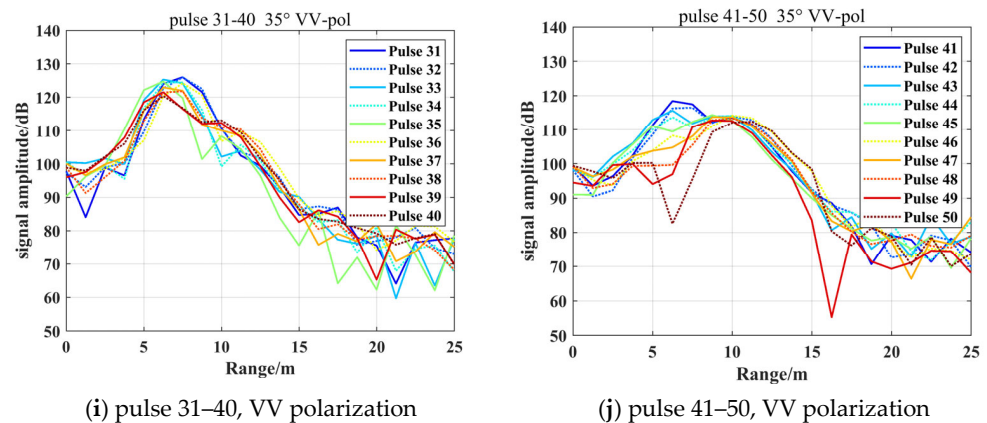(**e**) pulse 41–50, HH polarization

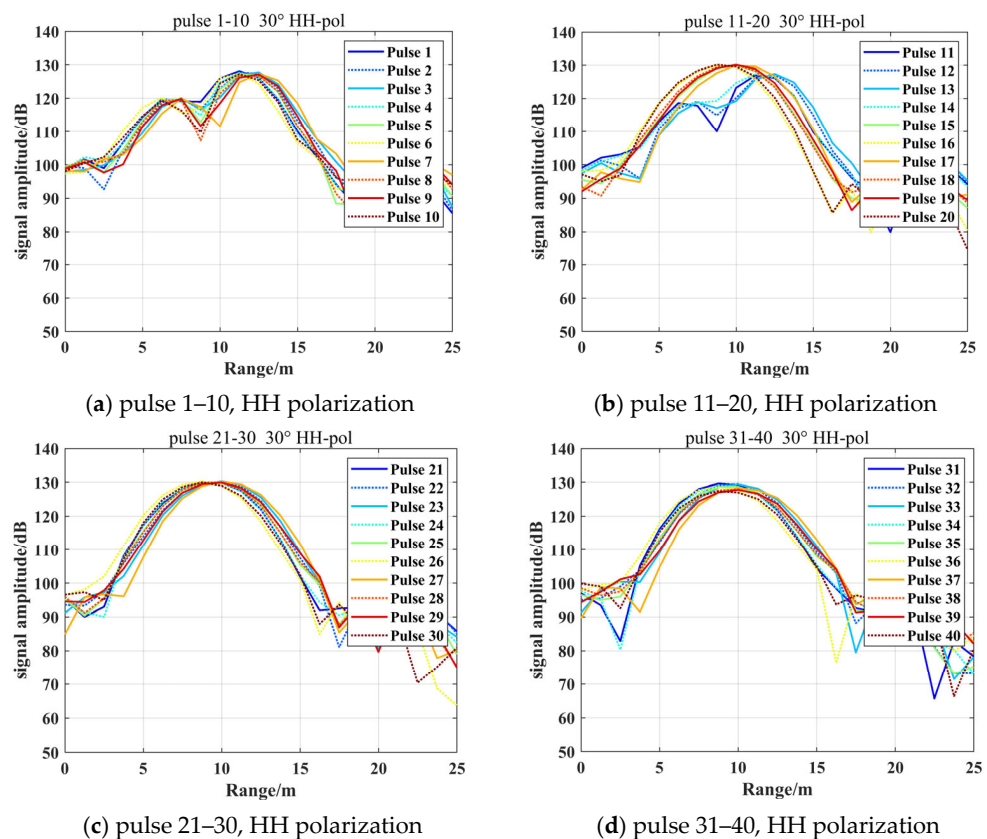(**f**) pulse 1–10, VV polarization

(**g**) pulse 11–20, VV polarization

(**h**) pulse 21–30, VV polarization

Figure 12. *Cont.*

(**i**) pulse 31–40, VV polarization

(**j**) pulse 41–50, VV polarization
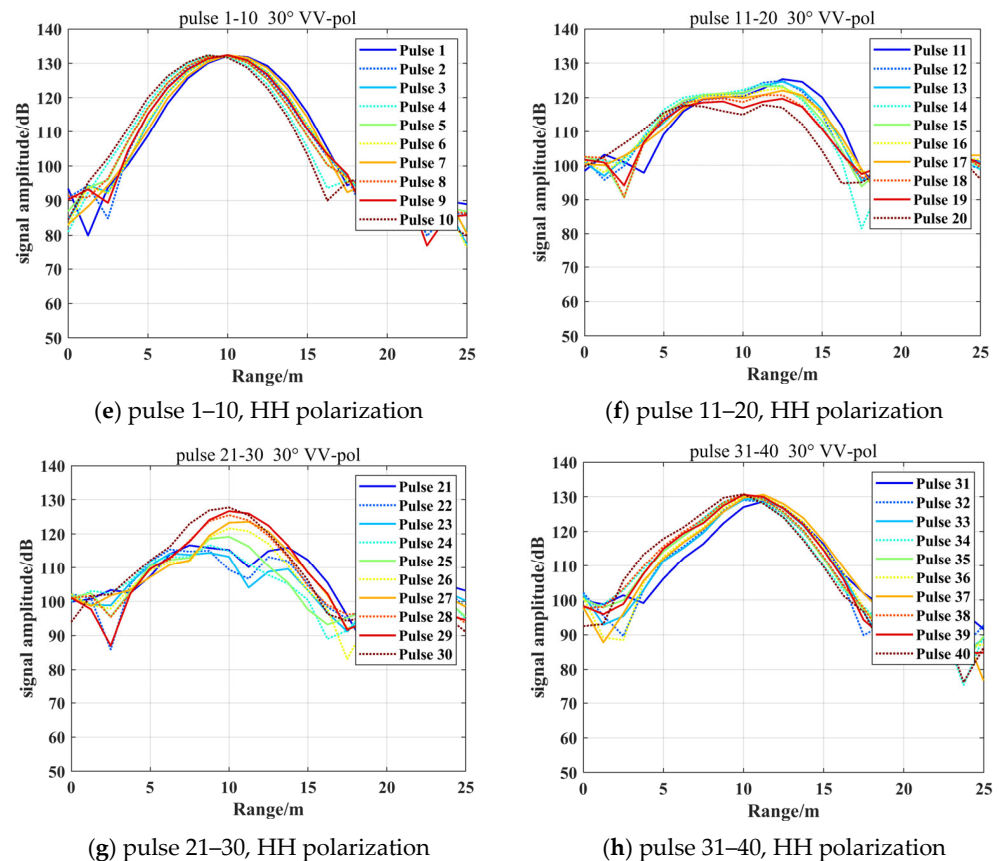
Figure 12. Sea echo of different pulses in a single observation sample with 35° incidence: (**a**–**e**) 35° incidence, HH polarization, windspeed = 7.5 m/s and (**f**–**j**): 35° incidence, VV polarization, windspeed = 8.3 m/s.

We also provided observations under similar sea-motion conditions (8.6 m/s for HH polarization and 8.1 m/s for VV polarizations) at an incidence angle of 30°, as shown in Figure 13. A bimodal signal also emerged for a wind speed of 8.6 m/s under HH polarization during short-duration observation (10 ms), leading to occasional and transient decreases in the scattering coefficient during high temporal resolution observations. We conducted a statistical analysis of the proportion of bimodal patterns through 25,000 samples over long-term observations (20 s) and discovered that, during high-resolution observations, the probability of VV polarization exhibiting bimodal patterns increased with the incidence angle, as shown in Table 3. This can explain why the backscatter coefficient in HH polarization is close to that in VV polarization at an incident angle of 30° but surpassed for the 35° observation.

(**a**) pulse 1–10, HH polarization

(**b**) pulse 11–20, HH polarization

(**c**) pulse 21–30, HH polarization

(**d**) pulse 31–40, HH polarization

Figure 13. *Cont.*

(**e**) pulse 1–10, HH polarization

(**f**) pulse 11–20, HH polarization

(**g**) pulse 21–30, HH polarization

(**h**) pulse 31–40, HH polarization

Figure 13. Sea echo of different pulses in a single observation sample with 30° incidence: (**a**–**d**) HH polarization, windspeed = 8.6 m/s and (**e**–**h**) VV polarization, windspeed = 8.1 m/s.

Figure 14 shows the sea echo amplitudes of different pulses with 45° incidence in an observation sample under VV polarization. As can be seen from the figure, for pulses 1–10, the sea surface echo exhibits a single-peak signal, then gradually transitions to a bimodal pattern for pulses 11–20. For pulses 21–30, the sea surface echo signal transitions from a one peak signal to a bimodal pattern with a slight shift in the corresponding slant range. For pulses 31–40, it gradually changes from a double-back to a single peak, with the energy of the double peak being approximately 18 dB lower than that of the single peak. For pulses 41–50, the sea surface echo initially presents as a single peak, later developing into a single peak with a smaller side-lobe peak, then changes back to a single peak. These changes indicate that, within an observation period of 10 ms, the ocean waves undergo rapid variations. In other words, these signal changes correspond to the wave motion, breaking, and other variations of the waves.

We have also conducted a statistical analysis on the short-term and long-term signal characteristics under HH and VV polarizations at an incidence angle of 50.5°. We found that as the incidence angle increases, the bimodal or even trimodal signal features for both polarizations become pronounced, as shown in Figure 15. We attribute this to the rapid changes in the angle between the incident direction of the radar wave and the locally inclined surface, especially for high wind speed and large incident angles. After statistical observation of multiple samples, we can conclude that for high-resolution, fixed-point observations of sea surface in the Ka-band, the sea echo becomes very sensitive to rapid wave motion, exhibiting complex scattering characteristics such as multiple peaks and reduced scattering energy at high windspeed and large incident angles.
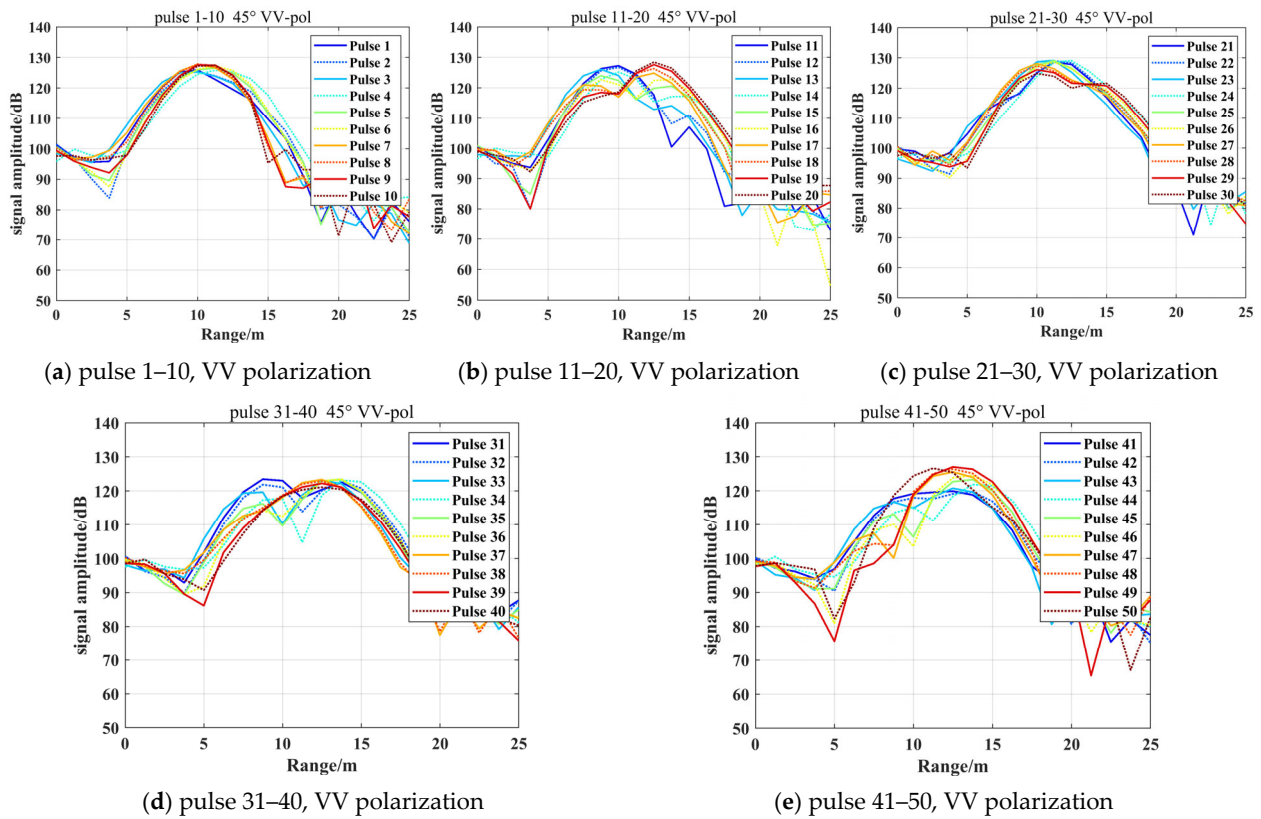
Figure 14. Signal amplitude of sea echo with different pulses with 45° incidence.
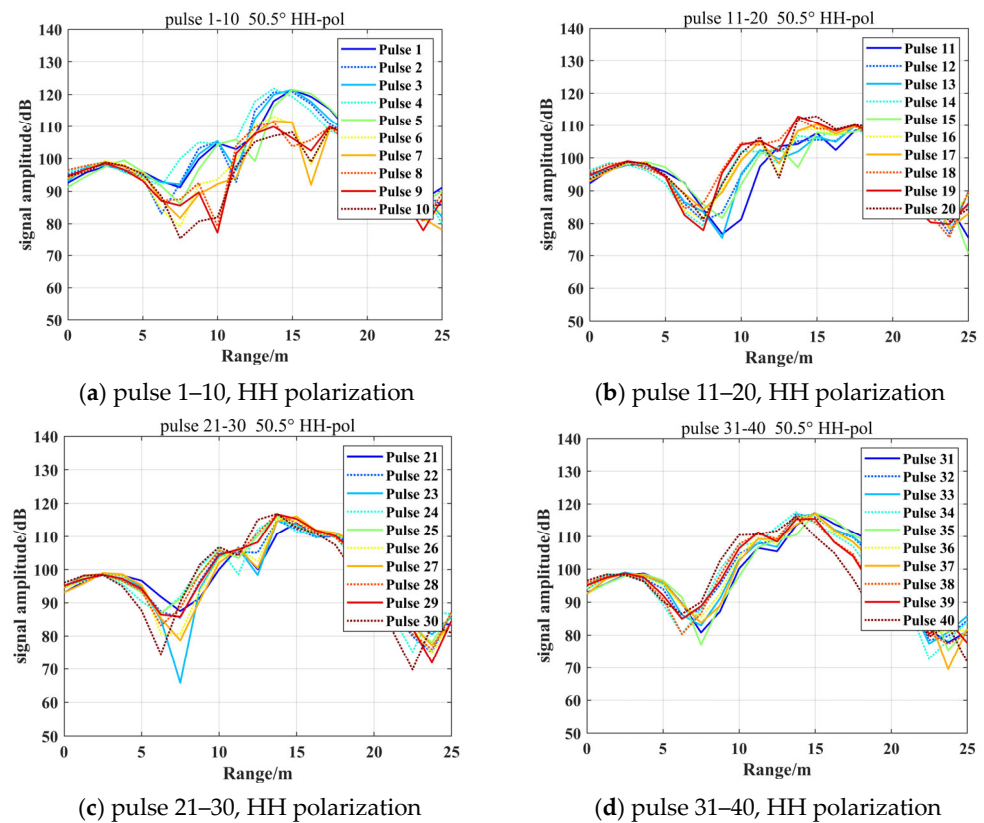
(**a**) pulse 1–10, VV polarization (**b**) pulse 11–20, VV polarization (**c**) pulse 21–30, VV polarization

(**d**) pulse 31–40, VV polarization (**e**) pulse 41–50, VV polarization

(**a**) pulse 1–10, HH polarization (**b**) pulse 11–20, HH polarization

(**c**) pulse 21–30, HH polarization (**d**) pulse 31–40, HH polarization

Figure 15. *Cont*.

(**e**) pulse 41–50, HH polarization

(**f**) pulse 1–10, VV polarization

(**g**) pulse 11–20, VV polarization

(**h**) pulse 21–30, VV polarization
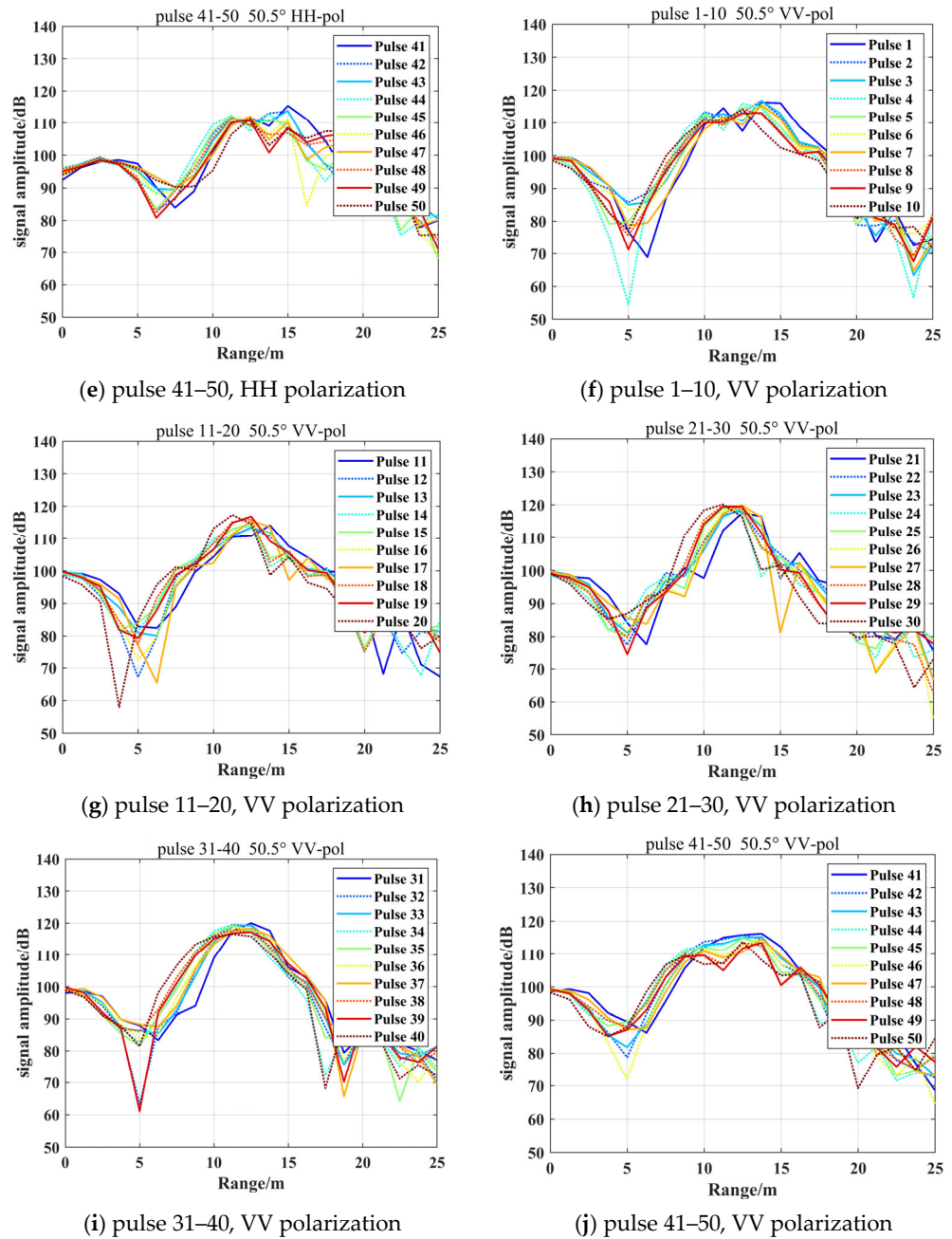
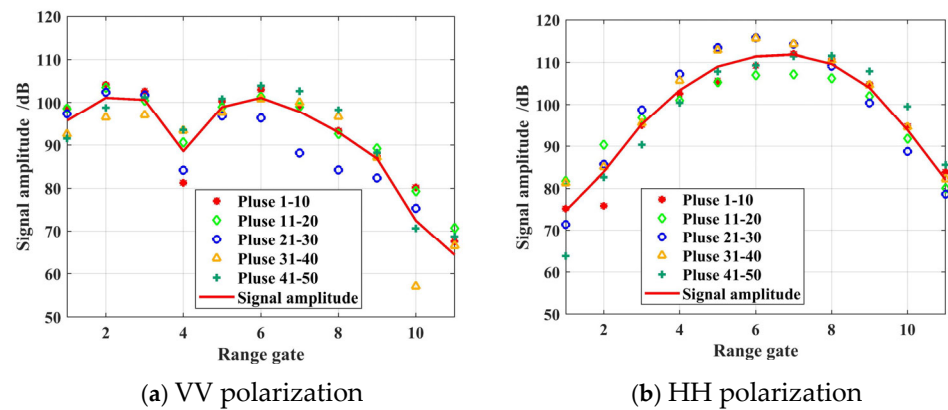(**i**) pulse 31–40, VV polarization

(**j**) pulse 41–50, VV polarization

Figure 15. Sea echo of different pulses in a single observation sample with a 50.5° incidence: (**a–e**) HH polarization, windspeed = 7.7 m/s and (**f–g**) VV polarization, windspeed = 5.9 m/s.

Figure 16 shows the signal amplitude of the sea echo with different range gates with a 45° incidence under VV polarization. Gate 6 is at the center of the beam illumination, where the backscattering coefficient is the highest. Five range gates were selected before and after Gate 6. The Doppler velocity is shown in Figure 17b. We also show the Doppler velocity at a 45° incidence both in the HH and VV polarizations with similar wind speeds in Figure 17.

From Figure 16, it can be seen that at a 45° incidence angle and similar wind speeds, the sea surface echo under HH polarization exhibits a more stable single peak compared to that under VV polarization. Further analysis of the Doppler velocity in Figure 17 reveals that the Doppler velocity can reflect rapid changes in ocean wave motion. Within an observation period of 10 ms, where the sea surface echoes exhibit a solitary peak, the Doppler velocity fluctuations across various range gates manifest as relatively mild. Conversely, when the

beam's center detects rapid oceanic changes, abrupt changes, or outliers in the Doppler velocity, fluctuations will occur near the corresponding range gate.

(**a**) VV polarization

(**b**) HH polarization

Figure 16. Sea echoes of different pulses with different range gates with a 45° incidence.

(**a**)

(**b**)
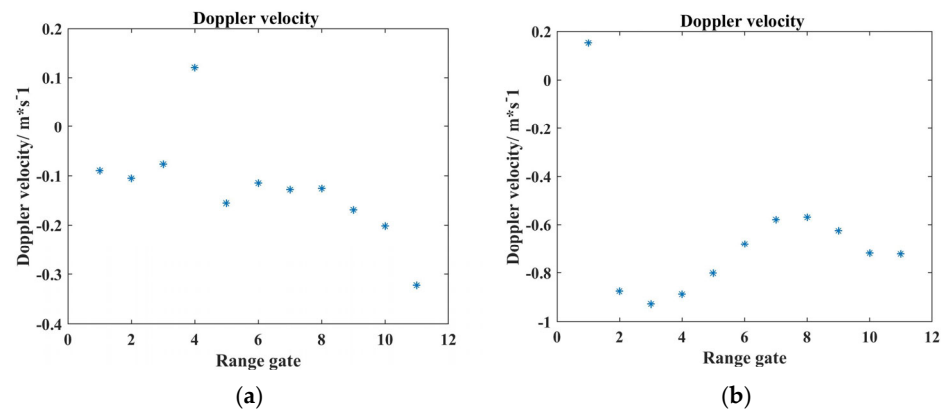
Figure 17. Doppler velocity with 45° incidence. (**a**) VV polarization; (**b**) HH polarization.

5. Conclusions

This experiment designed a high temporal and spatial resolution radar system for sea observation and conducted measurements in the open sea under different polarizations, incident angles, and wind speeds. In contrast to traditional observation for large sea areas, this high-resolution radar system focused on fixed-point observations of the fine structure of the ocean's surface. During a 200-s observation of the backscatter coefficient at the beam center, an intriguing revelation emerged: at the medium incidence angle, the backscatter coefficient in HH polarization is close to (or even surpasses) that found in VV polarization within a wind speed range of 7.1 to 8.6 m/s. Further analysis of the 10-ms observation samples revealed that the sea echo in VV polarization is more sensitive to wave motion, exhibiting more complex scattering characteristics such as multiple peaks and reduced scattering energy at high wind speed and large incident angles. Furthermore, the Doppler velocity analysis confirmed that rapid ocean wave changes are detectable within short observation periods, particularly under VV polarization.

In summary, the radar system has the ability to detect the sea surface with high temporal and spatial resolution, and the measured signals hold significant potential for estimating the sea state and surface currents, elucidating and inverting fast-evolving oceanic phenomena.

Author Contributions: Conceptualization, X.S., L.L. and Z.W.; methodology, X.S., X.Z. and L.L.; formal analysis, X.S. and X.Z.; funding acquisition, X.S. and X.Z.; investigation, X.Z.; writing—original draft, X.Z.; writing—review and editing, X.Z. and X.S. All authors have read and agreed to the published version of the manuscript.

Conflicts of Interest: The authors declare no conflicts of interest.

References

1. Cai, Y.; Cheng, X.; Sun, G. A Review of Development of Radar Altimeter and Its Applications. *Remote Sens.* **2006**, *4*, 74–78.
2. Mouche, A.A.; Collard, F.; Chapron, B.; Dagestad, K.F.; Guitton, G.; Johannessen, J.A.; Kerbaol, V.; Hansen, M.W. On the use of doppler shift for sea surface wind retrieval from SAR. *IEEE Trans. Geosci. Remote Sens.* **2012**, *50*, 2901–2909. [CrossRef]
3. Francesco, S.; Lugni, C.; Ludeno, G.; Arturi, D.; Uttieri MBuonocore BZambianchi, E.; Budillon, G. REMOCEAN: A Flexible X-Band Radar System for Sea-State Monitoring and Surface Current Estimation. *IEEE Geosci. Remote Sens. Lett.* **2012**, *9*, 822–826.
4. Fan, Y.; Chen, D.; Chen, S.; Su, J.; Tao, M.; Guo, Z.; Wang, L. Weak Target Detection Based on Full-Polarization Scattering Features under Sea Clutter Background. *Remote Sens.* **2024**, *16*, 2987. [CrossRef]
5. Liu, X.; Kong, W.; Sun, H.; Lu, Y. Performance Analysis of Ku/Ka Dual-Band SAR Altimeter from an Airborne Experiment over South China Sea. *Remote Sens.* **2022**, *14*, 2362. [CrossRef]
6. Sapp, J.; Jelenak, Z.; Chang, P.; Carswell, J.R.; Pollard, B.; Theg, A. Near-Real-Time Significant Wave Heights in Hurricanes from a New Airborne KA-Band Interferometric Altimeter. In Proceedings of the 2021 IEEE International Geoscience and Remote Sensing Symposium IGARSS, Brussels, Belgium, 11–16 July 2021; pp. 7426–7429.
7. Guo, H.; Wan, X.; Wang, H. Validation of Just-Released SWOT L2 KaRIn Beta Prevalidated Data Based on Restore the Marine Gravity Field and Its Application. *IEEE J. Sel. Top. Appl. Earth Obs. Remote Sens.* **2024**, *17*, 7878–7887. [CrossRef]
8. Rodríguez-Morales, F.; Li, J.; Leuschen, C.; Hvidegaard, S.M.; Forsberg, R. Airborne Altimetry Measurements in the Arctic Using a Compact Multi-Band Radar System: Initial Results. In Proceedings of the IGARSS 2020—2020 IEEE International Geoscience and Remote Sensing Symposium, Waikoloa, HI, USA, 26 September–2 October 2020; pp. 3019–3022.
9. Stiles, B.W.; Fore, A.G.; Bohe, A.; Chen, A.C.; Chen, C.W.; Molero, B.; Dubois, P. Ocean Surface Wind Speed Retrieval for SWOT Ka-band Radar Interferometer. In Proceedings of the IGARSS 2024—2024 IEEE International Geoscience and Remote Sensing Symposium, Athens, Greece, 7–12 July 2024; pp. 1422–1425.
10. Polverari, F.; Wineteer, A.; Rodriguez, E.; Perkovic-Martin, D.; Siqueira, P.; Farra, J.T.; Adam, J.M.; Edson, J. Towards a Characterization of the Ka-Band Ocean Surface Backscattering Mechanisms. In Proceedings of the 2021 IEEE International Geoscience and Remote Sensing Symposium IGARSS, Brussels, Belgium, 11–16 July 2021; pp. 7529–7532.
11. Polverari, F.; Wineteer, A.; Rodríguez, E.; Perkovic-Martin, D.; Siqueira, P.; Farrar, J.T.; Adam, M.; Closa Tarrés, M.; Edson, J.B. A Ka-Band Wind Geophysical Model Function Using Doppler Scatterometer Measurements from the Air-Sea Inter-action Tower Experiment. *Remote Sens.* **2022**, *14*, 2067. [CrossRef]
12. Rodríguez, E. On the Optimal Design of Doppler Scatterometers. *Remote Sens.* **2018**, *10*, 1765. [CrossRef]
13. Wineteer, A.; Perkovic-Martin, D.; Monje, R.; Rodríguez, E.; Gál, T.; Niamsuwan, N.; Nicaise, F.; Srinivasan, K.; Baldi, C.; Majurec, N.; et al. Measuring Winds and Currents with Ka-Band Doppler Scatterometry: An Airborne Implementation and Progress towards a Spaceborne Mission. *Remote Sens.* **2020**, *12*, 1021. [CrossRef]
14. Fu, L.L.; Alsdorf, D.; Morrw, R.; Rodriguez, E.; Mognard, N. *Swot: The Surface Water and Ocean Topography Mission: Wideswath Altimetric Elevation on Earth*; Tech. Rep. JPL-Publication 12-05; Jet Propuls. Lab.: Pasadena, CA, USA, 2012; pp. 85–91.
15. Qiu, Z.; Ma, C.; Wang, Y.; Yu, F.; Zhao, C.; Sun, H.; Zhao, S.; Yang, L.; Tang, J.; Chen, G. Improving Sea Surface Height Reconstruction by Simultaneous Ku- and Ka-Band Near-Nadir Single-Pass Interferometric SAR Altimeter. *IEEE Trans. Geosci. Remote Sens.* **2023**, *61*, 5209614. [CrossRef]
16. Chen, G.; Tang, J.; Zhao, C.; Wu, S.; Yu, F.; Ma, C.; Xu, Y.; Chen, W.; Zhang, Y.; Liu, J.; et al. Concept design of the 'Guanlan' science mission: China's novel contribution to space oceanography. *Front. Mar. Sci.* **2019**, *6*, 194. [CrossRef]
17. Yurovsky, Y.Y.; Kudryavtsev, V.N.; Chapron, B. Simultaneous radar and video observations of the sea surface in field conditions. In Proceedings of the 2017 Progress in Electromagnetics Research Symposium—Spring (PIERS), St. Petersburg, Russia, 22–25 May 2017; pp. 2559–2565.
18. Yurovsky, Y.Y.; Kudryavtsev, V.N.; Grodsky, S.A.; Chapron, B. Ka-Band Doppler Scatterometry: A Strong Wind Case Study. *Remote Sens.* **2022**, *14*, 1348. [CrossRef]
19. Yurovsky, Y.Y.; Kudryavtsev, V.N.; Grodsky, S.A.; Chapron, B. Ka-Band Radar Backscattering from Breaking Wind Waves. In Proceedings of the 2021 IEEE International Geoscience and Remote Sensing Symposium IGARSS, Brussels, Belgium, 11–16 July 2021; pp. 7394–7397.
20. Yurovsky, Y.Y.; Kudryavtsev, V.N.; Grodsky, S.A.; Chapron, B. Ka-Band Radar Cross-Section of Breaking Wind Waves. *Remote Sens.* **2021**, *13*, 1929. [CrossRef]

21. Yurovsky, Y.Y.; Kudryavtsev, V.N.; Grodsky, S.A.; Chapron, B. On Doppler Shifts of Breaking Waves. *Remote Sens.* **2023**, *15*, 1824. [CrossRef]
22. Zhang, X.; Wu, Z.-S.; Su, X. Electromagnetic Scattering from Deterministic Sea Surface with Oceanic Internal Waves via the Variable-Coefficient Gardener Model. *IEEE J. Sel. Top. Appl. Earth Obs. Remote Sens.* **2018**, *11*, 355–366. [CrossRef]
23. Zhang, X.; Su, X.; Wu, Z. A volume-surface composite scattering model for nonlinear ocean surface with breaking waves and foam layers under high wind conditions. *Prog. Electromagn. Res. B* **2019**, *85*, 125–142. [CrossRef]
24. Yurovsky, Y.Y.; Kudryavtsev, V.N.; Grodsky, S.A.; Chapron, B. Ka-Band Dual Copolarized Empirical Model for the Sea Surface Radar Cross Section. *IEEE Trans. Geosci. Remote Sens.* **2017**, *55*, 1629–1647. [CrossRef]
25. Wei, Y.; Guo, L.; Li, J. Numerical simulation and analysis of the spiky sea clutter from the sea surface with breaking waves. *IEEE Trans. Antennas Propag.* **2015**, *63*, 4983–4994. [CrossRef]
26. Trizna, D.B. A model for Brewster angle damping and multipath effects on the microwave radar sea echo at low grazing angles. *IEEE Trans. Geosci. Remote Sens.* **1997**, *35*, 1232–1244. [CrossRef]
27. Wu, Z.S.; Zhang, J.P.; Guo, L.X.; Zhou, P. An improved two-scale model with volume scattering for the dynamic ocean surface. *Prog. Electromagn. Res.* **2009**, *89*, 39–56. [CrossRef]
28. Churyumov, A.N.; Kravtsov, Y.A. Microwave backscatter from mesoscale breaking waves on the sea surface. *Waves Random Media* **2000**, *10*, 1–15. [CrossRef]